# Size-Dependent Lattice Structure and Confinement Properties in $CsPbI_3$ Perovskite Nanocrystals: Negative Surface Energy for Stabilization

**Authors:** Qian Zhao,[1,2,3] Abhijit Hazarika,[2] Laura T. Schelhas,[4] Jun Liu,[2] E. Ashley Gaulding,[2] Guoran Li,[3] Minghui Zhang,[1] Michael F. Toney,[4] Peter C. Sercel,[5] Joseph M. Luther[2]*

**Affiliations:**

[1]College of Chemistry, Nankai University, Tianjin 300071, China

[2]National Renewable Energy Laboratory, Golden, CO 80401, USA

[3]Institute of New Energy Material Chemistry, Nankai University, Tianjin 300350, China

[4]SLAC National Accelerator Laboratory, Menlo Park, CA 94025, USA

[5]T. J. Watson Laboratory of Applied Physics, California Institute of Technology, Pasadena, CA 91125, USA

*Correspondence to: joey.luther@nrel.gov

**Methods section:**

**Materials.** Oleylamine (OAm; technical grade, 70%), 1-octadecene (ODE; technical grade, 90%), Cesium carbonate ($Cs_2CO_3$; 99.9%), oleic acid (OA; technical grade, 90%), methyl acetate (MeOAc; anhydrous, 99.5%), octane (anhydrous, ≥99%), lead nitrate ($Pb(NO_3)_2$; 99.999%), hexane (reagent grade, ≥95%), formamidinium acetate (FA-acetate, 99%) were purchased from Sigma-Aldrich and used as received unless otherwise specified.

**$CsPbI_3$ QD synthesis.** The synthesis was performed following the method reported in our previous publications with slight modification.[1,2] First, 20 mL of ODE is mixed with 1.25 mL of OA containing 0.407 g of $Cs_2CO_3$. This was degassed at 120°C for 20 min under vacuum in a three-neck flask to form Cs-oleate. The Cs-oleate precursor was kept under $N_2$ instead of vacuum after $Cs_2CO_3$ was completely dissolved in the solution. Then the $PbI_2$ precursor was formed by mixing 0.5 g of $PbI_2$ and 25 mL of ODE in a three-neck flask and heated at 120°C for 20 min under vacuum. A preheated mixture of OA and OAm (135°C, 2.5 mL each) was transferred into the $PbI_2$ solution that was kept at 120°C under vacuum. After the $PbI_2$ completely dissolved in the solution, the reaction flask was heated to the desired temperature (140, 160, or 180°C) under flowing $N_2$. Then 2 mL of the Cs-oleate precursor was swiftly injected into the reaction flask. In general, smaller nanocrystals are obtained with lower growth and larger are obtained with higher temperature, but some sizes overlap this trend when using the size selective precipitation. Immediately after the reaction, the mixture was quenched by submerging the flask into an ice bath within 3 s after the injection. After cooling to room temperature, 70 mL of MeOAc was added into the colloidal solution and the mixed solution was centrifuged at 7500 rpm for 5 min.

The precipitated $CsPbI_3$ QDs were dispersed in 10 mL of hexane. The purified QDs can be stored for over a month without noticeable degradation.

**$CsPbI_3$ QDs size-selective precipitation and purification.** MeOAc was added in the initial $CsPbI_3$ QD solution in a volume ratio of 1 : 3. After centrifugation at 7500 rpm for 5 min, larger NCs were precipitated. The supernatant was decanted and MeOAc was added to it in a volume ratio of 1 : 3 and the mixed solution was centrifuged at 7500 rpm for 5 min, producing another batch of precipitates. This process was repeated multiple times until there is no obvious precipitation of QDs from the supernatant. The resulting precipitate from every batch was redispersed in 3 mL of hexane. The obtained QD solution was centrifuged at 7500 rpm for 5 min and the precipitate was discarded. The supernatant was filtered through a 0.45 μm nylon filter and then kept in a sealed vial for characterization.

**$CsPbI_3$ QDs Characterization.** TEM images were obtained using a FEI Tecnai F20 electron microscope with 200 kV accelerating voltage. Ultraviolet-visible absorption spectra were measured using a Shimadzu UV-3600 UV-vis-NIR spectrophotometer. Steady-state photoluminescence (PL) spectra were recorded with a 450 nm excitation by a Horiba Jobin Yvon fluoromax-4 spectrophotometer. Powder X-ray diffraction (XRD) data were obtained using a Rigaku's DMax diffractometer with Cu-kα radiation (wavelength 1.5406 Å) operated at 40 kV and 250 mA, with a step width of 0.02° and a count time of 1.0 s in the $2\theta$ range from 3° to 70°. Reference markers for XRD are calculated with Mercury software employing the reported crystallographic information[3]. The Rietveld refinement of the XRD data was performed using the TOPAS-Academic software package.

**Table S1.** Physical parameters of $CsPbI_3$ QD samples. The mean sizes and standard deviation are determined assuming a Gaussian distribution from TEM analysis. The 1st Excitonic transition energy and Stokes' shift are obtained from the corresponding UV and PL spectra for each size of QDs.

| Mean size (nm) | Standard deviation (nm) | Size dispersion (%) | 1st Excitonic transition energy (meV) | Stokes' shift (meV) |
|---|---|---|---|---|
| 5.2 | 0.6 | 11.5 | 1955 | 42 |
| 5.7 | 0.7 | 12.3 | 1946 | 42 |
| 6.3 | 0.7 | 11.1 | 1925 | 38 |
| 7.2 | 0.8 | 11.1 | 1907 | 49 |
| 7.6 | 0.8 | 10.5 | 1887 | 39 |
| 8.5 | 0.9 | 10.6 | 1861 | 28 |
| 9.2 | 1 | 10.8 | 1847 | 30 |
| 13.9 | 2.2 | 15.8 | 1842 | 38 |
| 15.3 | 1.7 | 11.1 | 1834 | 42 |

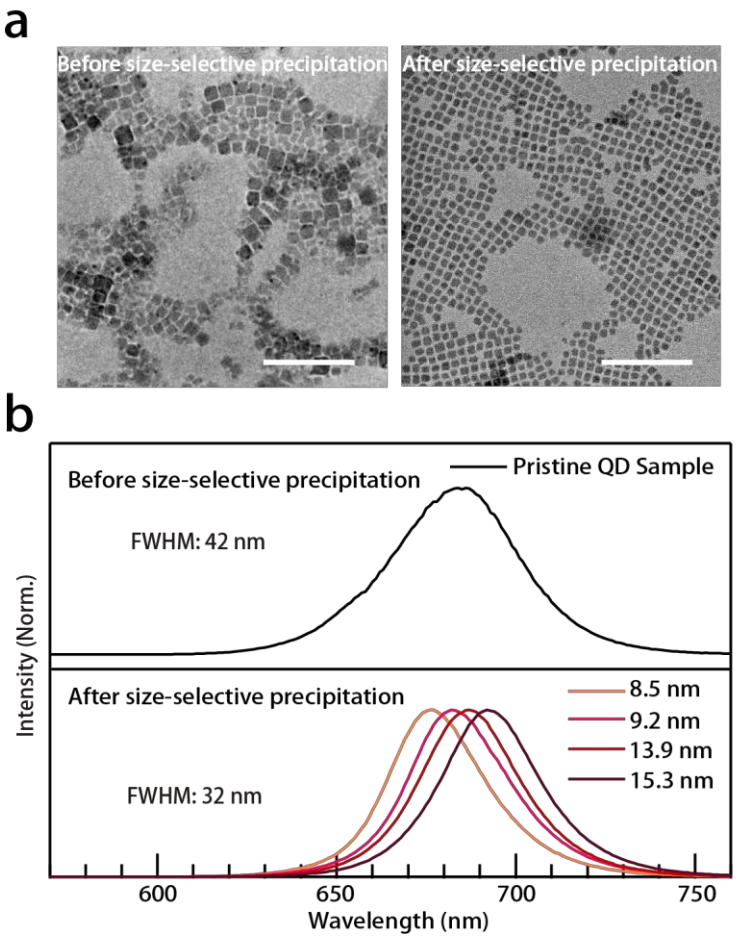


**Figure S1.** (a) TEM images of $CsPbI_3$ QD samples before and after size-selective precipitation. The mean size of QD sample (right) is 8.5 nm after size-selective precipitation. The pristine QDs (left) were synthesized at 180°C. The scale bars in TEM images are 100 nm. (b) PL spectra of $CsPbI_3$ QD samples before and after size-selective precipitation. The starting QD sample was separated into four fractions with mean sizes of 8.5 ± 0.9, 9.2 ± 1.0, 13.9 ± 2.2 and 15.3 ± 1.7 nm, respectively. The average FWHM of PL peaks for QD sample decreases from 42 to 32 nm after size-selective precipitation.

**Table S2.** FWHM from PL spectra of perovskite QD samples with different sizes.

| $CsPbI_3$ in this work | | $CsPbI_3$ from other works | | $CsPbBr_3$ from other works | |
|---|---|---|---|---|---|
| **Mean size (nm)** | **FWHM (nm)** | **Mean size (nm)** | **FWHM (nm)** | **Mean size (nm)** | **FWHM (nm)** |
| 5.2 | 49 | 6.5[4] | 58 | 4.5[5] | 15 |
| 5.7 | 50 | 9.6[6] | 39 | 5.5[7] | 24 |
| 6.3 | 45 | 10[8] | 45 | 6.4[5] | 24 |
| 7.2 | 36 | 10.8[4] | 44 | 7.45[9] | 18 |
| 7.6 | 34 | 11.2[10] | 38 | 9.4[11] | 25 |
| 8.5 | 32 | 11.8[12] | 41 | 11[13] | 18 |
| 9.2 | 33 | 11.8[4] | 46 | 13.7[7] | 17 |
| 13.9 | 32 | 13[14] | 42 | 12-15[15] | 20 |
| 15.3 | 32 | 20[16] | 40 | 15[17] | 20 |

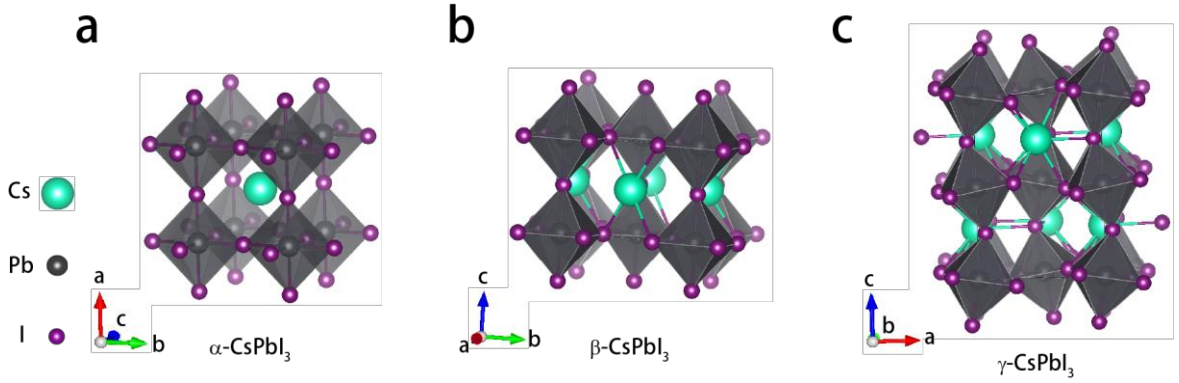


**Figure S2** (a-c) Crystal structure model of *α*, *β* and *γ* phases for $CsPbI_3$ QDs exhibited with different angles, respectively. The bulk lattice constants of the *γ* phase at room temperature are 8.5766 Å for *a*, 8.8561 Å for *b*, and 12.4722 Å for *c*.[18]

**Table S3.** Rietveld refinement parameters of $CsPbI_3$ QD samples with the mean size of 5.7 and 15.3 nm. All parameters for the model of $\alpha$, $\beta$ and $\gamma$ phases were obtained at 300K. The experimental data were taken using a Rigaku's DMax diffractometer with Cu-kα radiation possessing a wavelength of 1.5406 Å.

| **QD size (nm)** | **5.7** | | | | | | | | |
|---|---|---|---|---|---|---|---|---|---|
| **Crystal system** | Cubic ($\alpha$ phase) | | | Tetragonal ($\beta$ phase) | | | Orthorhombic ($\gamma$ phase) | | |
| **Space Group** | *Pm-3m* | | | *P4/mbm* | | | *Pbnm* | | |
| **Lattice constant** | $a$=6.223(3) | | | $a$=8.804(15); $c$=6.228(18) | | | $a$=8.591(6); $b$=9.038(7); $c$=12.461(8) | | |
| **$R_{wp}$** | 14.05 | | | 13.13 | | | 10.85 | | |
| | **Atomic position** | | | | | | | | |
| Pb | 0 | 0 | 0 | 0 | 0 | 0 | 0 | 0 | 1/2 |
| Cs | 1/2 | 1/2 | 1/2 | -1/2 | 0 | 1/2 | -0.0165 | 0.4451 | 1/4 |
| I1 | 0 | 0 | 1/2 | 0 | 0 | 1/2 | -0.209(1) | 0.294(1) | 0.520(1) |
| I2 | N/A | N/A | N/A | -0.217(1) | 0.282(1) | 0 | -0.022(3) | 0.017(2) | 3/4 |
| **QD size (nm)** | **15.3** | | | | | | | | |
| **Crystal system** | Cubic ($\alpha$ phase) | | | Tetragonal ($\beta$ phase) | | | Orthorhombic ($\gamma$ phase) | | |
| **Space Group** | *Pm-3m* | | | *P4/mbm* | | | *Pbnm* | | |
| **Lattice constant** | $a$=6.211(2) | | | $a$=8.776(8); $c$=6.214(10) | | | $a$=8.633(6); $b$=8.844(2); $c$=12.482(2) | | |
| **$R_{wp}$** | 20.11 | | | 16.91 | | | 10.73 | | |
| | **Atomic position** | | | | | | | | |
| Pb | 0 | 0 | 0 | 0 | 0 | 0 | 0 | 0 | 1/2 |
| Cs | 1/2 | 1/2 | 1/2 | -1/2 | 0 | 1/2 | -0.0165 | 0.4451 | 1/4 |
| I1 | 0 | 0 | 1/2 | 0 | 0 | 1/2 | 0.199(1) | 0.299(1) | 0.524(1) |
| I2 | N/A | N/A | N/A | -0.217(1) | 0.282(1) | 0 | -0.057(1) | 0.001(1) | 3/4 |

**Table S4.** Lattice constants of the QD samples. The lattice constants are calculated based on the Rietveld refinement with $\gamma$ phase. Some of samples with the same size were synthesized from different batches.

| Mean size of the QD sample (nm) | a | | b | | c | |
|---|---|---|---|---|---|---|
| | Value (Å) | Error range (±) | Value (Å) | Error range (±) | Value (Å) | Error range (±) |
| 5.67 | 8.6258 | 0.0066 | 8.9800 | 0.0063 | 12.4710 | 0.0091 |
| 5.70 | 8.5504 | 0.0071 | 9.0809 | 0.0080 | 12.4585 | 0.0093 |
| 5.70 | 8.5920 | 0.0067 | 9.0389 | 0.0076 | 12.4681 | 0.0089 |
| 5.90 | 8.6167 | 0.0062 | 8.9928 | 0.0063 | 12.4708 | 0.0084 |
| 6.20 | 8.5365 | 0.0088 | 9.0897 | 0.0098 | 12.4614 | 0.0113 |
| 6.20 | 8.5288 | 0.0087 | 9.0784 | 0.0094 | 12.4394 | 0.0112 |
| 6.28 | 8.5011 | 0.0085 | 9.0553 | 0.0089 | 12.4492 | 0.0119 |
| 6.80 | 8.7064 | 0.0088 | 8.8394 | 0.0060 | 12.5301 | 0.0080 |
| 7.13 | 8.6477 | 0.0062 | 8.9504 | 0.0061 | 12.4733 | 0.0085 |
| 7.30 | 8.6836 | 0.0069 | 8.9288 | 0.0067 | 12.4700 | 0.0096 |
| 7.30 | 8.6238 | 0.0062 | 8.9611 | 0.0066 | 12.4468 | 0.0084 |
| 7.50 | 8.6366 | 0.0071 | 8.9432 | 0.0068 | 12.4505 | 0.0099 |
| 7.60 | 8.6701 | 0.0060 | 8.9403 | 0.0057 | 12.4655 | 0.0079 |
| 8.07 | 8.6711 | 0.0043 | 8.8107 | 0.0037 | 12.5495 | 0.0041 |
| 8.47 | 8.7014 | 0.0053 | 8.8715 | 0.0044 | 12.4877 | 0.0068 |
| 9.22 | 8.6801 | 0.0035 | 8.8520 | 0.0031 | 12.5087 | 0.0042 |
| 15.20 | 8.6333 | 0.0022 | 8.8435 | 0.0021 | 12.4814 | 0.0025 |
| 15.28 | 8.6184 | 0.0016 | 8.8709 | 0.0016 | 12.5125 | 0.0019 |

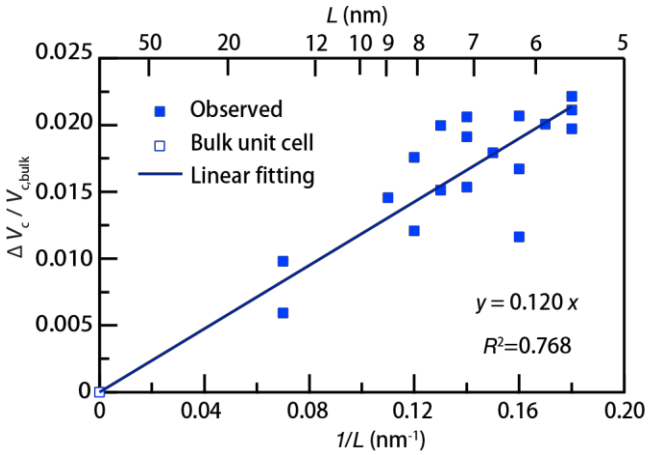


**Figure S3.** Unit cell volume dilatation relative to the bulk unstrained unit cell volume plotted versus 1/*L*. Unit cell volumes for different sized nanoparticles (NCs) are computed using the lattice constant data in Table S4. The unit cell volume of the bulk (hollow square) unstrained crystal is computed with the bulk lattice constants from Sutton and co-workers.[18] The best fit slope of the curve is $m = 0.12$ nm.

**Surface energy calculations**

The surface energy (surface stress) of a nanoparticle is defined as the energy required to create unit surface area or as the partial of the nanoparticle free energy ($G$) with respect to its surface area ($A$). For a spherical nanoparticle of radius R, this has the well-known form as Eq. S1,

$$\Delta G = \gamma \Delta A = \frac{2\gamma}{R} \Delta V \quad \text{(S1)}$$

where $\gamma$ is the surface energy or surface stress, and the term $\frac{2\gamma}{R}$ is known as the capillary pressure. For nanoparticles of non-spherical shape, the capillary pressure is determined by the generalized capillary equation[19,20] (Eq. S2),

$$\Delta P = \gamma \frac{2}{3} \frac{A}{V} \quad \text{(S2)}$$

where $V$ is the volume of the nanoparticle and $\gamma$ is the area averaged surface stress. For a cube-shaped nanoparticle with edge length, $L$, this takes the form as Eq. S3,

$$\Delta P = \frac{4\gamma}{L} \quad \text{(S3)}$$

For positive surface stress, the capillary pressure compresses the nanoparticle, inducing lattice contraction; whereas for negative surface stress, it induces lattice expansion.[20] The resulting volume dilatation, which is equal to the volume dilatation of the lattice unit cell, is found using the bulk modulus, $B = -V\mathrm{d}P/\mathrm{d}V$ as Eq. 4,

$$\frac{\Delta V_c}{V_{c,bulk}} = -\frac{4\gamma}{B}\frac{1}{L} \quad \text{(S4)}$$

This relation predicts that the unit cell volume dilatation will be a linear function of the reciprocal of the nanocrystal size, *L*. Indeed, in Figure S3, the measured unit cell volume dilatation is plotted versus 1/*L*, shows the expected linear relationship. Thus, the surface energy can be determined from the slope of the volume dilatation vs 1/*L* shown in Figure S3 and shown in Eq. S5,

$$\gamma = -\frac{Bm}{4} \quad \text{(S5)}$$

where *m* is the slope of the plot of the volume dilatation vs 1/L. With the bulk modulus, *B* =16 GPa, calculated using density functional theory for $CsPbI_3$ in the cubic perovskite phase, and the slope, m = 0.12 nm, the surface energy for $CsPbI_3$ NCs made here and capped with oleate and oleylammonium ligands is found as $\gamma$ = -3.0 eV $nm^{-2}$. Using an average pseudo-cubic lattice constant of 0.622 nm, this corresponds to a surface energy of -1.2 eV per surface unit cell on a (100) surface face.

An alternate analysis was developed for non-spherical particles in terms of continuum elasticity theory by Huang et al.[21] In this model, the volume dilatation of a solid nanoparticle of a given size and non-spherical shape is determined in terms of the surface energy $\gamma$ and the bulk modulus, *B*, using a shape factor $\chi$ to approximate the effect of the non-spherical shape shown as Eq. S6.

$$\frac{\Delta V_c}{V_{c,bulk}} = -2\left(\frac{4\pi}{3}\right)^{\frac{1}{3}}\frac{\gamma}{\chi^{1/2}B}\frac{1}{L} \quad \text{(S6)}$$

Here, $\chi$ is an effective radius, defined as the radius of a spherical nanoparticle with the same volume as the nanoparticle under consideration, and $L = \sqrt[3]{V}$ where *V* is the nanoparticle volume. As in the simpler generalized capillary model, the volume dilatation is again predicted to be a linear function of the reciprocal of the nanocrystal size, *L*. For the case of a cube shaped nanocrystal, the shape factor is given by Eq. S7.

$$\chi = 2\left(\frac{3}{4\pi}\right)^{1/3} = 1.24 \quad \text{((S7)}$$

Using these factors, surface energy can be determined for a cube shaped NC from the slope of the volume dilatation vs 1/*L* shown in Figure S3, as Eq. S8,

$$\gamma = -\frac{1}{2}\left(\frac{3}{4\pi}\right)^{\frac{1}{3}}\chi^{1/2}Bm \quad \text{(S8)}$$

where $m$ is the slope of the plot of the volume dilatation vs $1/L$. This expression, like Eq. S5, predicts that the volume dilatation will be linear with respect to $1/L$ with a slope proportional to the surface energy.

In Table S5 we compare the values of the surface energy using Eq. S5 and Eq. S8, determined from the slope of the volume dilatation curve shown in Figure S3. The surface energy calculations are performed with the bulk modulus $B$ = 16 GPa for $\alpha$-$CsPbI_3$ calculated using density function theory reported by Jong and coworkers,[22] as well as $B$ = 19.8 GPa measured for the non-perovskite $\delta$-$CsPbI_3$ by Rakita et al.[23] The values calculated using the two methods are in good agreement.

**Table S5** Calculated values of ligand capped $CsPbI_3$ NC surface energy using the generalized capillary model[19] as Eq. S5, and the elasticity theory model[21] shown in Eq. S8. The value of the slope, $m$, determined by a linear fit to the data shown in Figure S3 is 0.12 nm.

| **Bulk modulus *B*** | **Capillary model** | **Elastic model** |
|---|---|---|
| 16 GPa[22] | -3.0 eV $nm^{-2}$ | -4.1 eV $nm^{-2}$ |
| 19.8 GPa[23] | -3.7 eV $nm^{-2}$ | -5.1 eV $nm^{-2}$ |

**Quantum confinement model calculations**

Within the effective mass approximation, the wavefunction of an exciton is (Eq. S9)[24,25]

$$\psi_{m,n}(\boldsymbol{r}_e, \boldsymbol{r}_h) = \Phi_{m,n}(\boldsymbol{r}_e, \boldsymbol{r}_h)\, f_{m,n}(\boldsymbol{r}_e, r_h) \quad \text{(S9)}$$

Here $\Phi_{m,n}$ ($\boldsymbol{r}_e$, $\boldsymbol{r}_h$) represents the band-edge basis cell-periodic functions for the exciton at the band extrema of conduction band ($m$) and valence band ($n$), while $f_{m,n}$ ($\boldsymbol{r}_e$, $\boldsymbol{r}_h$) is the envelope function for the exciton which describes the slowly varying electron and hole motion in the nanocrystal. The envelope functions $f_{m,n}$ ($\boldsymbol{r}_e$, $\boldsymbol{r}_h$) are found by solving the effective mass equation (Eq. S10) with appropriate boundary conditions.[24,25]

$$\widehat{H}^{eff}_{m',n';\,m,n} f_{m,n}(\boldsymbol{r}_e, \boldsymbol{r}_h) = E f_{m,n}(\boldsymbol{r}_e, \boldsymbol{r}_h) \quad \text{(S10)}$$

For a simple 2-fold degenerate band system such as the perovskites, the effective mass Hamiltonian for the exciton is given by Eq. S11,

$$\widehat{H}^{eff} = -\frac{\hbar^2}{2m_e}\nabla_e^2 - \frac{\hbar^2}{2m_e}\nabla_h^2 - U(\boldsymbol{r_e}, \boldsymbol{r_h})$$
$$= -\frac{\hbar^2}{2m_e}\nabla_e^2 - \frac{\hbar^2}{2m_e}\nabla_h^2 - \frac{e^2}{\epsilon|\boldsymbol{r_e}-\boldsymbol{r_h}|} \quad \text{(S11)}$$

In this expression, $m_e$ and $m_h$ are the effective masses at the band edge for the electron and hole, respectively. U($r_e$, $r_h$) represents the Coulomb interaction between the electron and the hole screened by the dielectric function ($\epsilon$). For a bulk semiconductor of volume $V$, that is large enough that quantum confinement effects are negligible, the solution to Eq. S10 is well known to correspond to a product of a hydrogenic function in the relative electron-hole coordinate, $r = r_e - r_h$, and a plane wave function corresponding to the center-of-mass coordinate of the exciton ($R$), where $\boldsymbol{R} = (m_e \boldsymbol{r}_e + m_h \boldsymbol{r}_h) = M$ and $M = m_e + m_h$, associated with wavevector $\boldsymbol{K}$. The exciton state with lowest energy relative motion has an envelope wavefunction given by Eq. S12,

$$f_{\boldsymbol{K};1s}(\boldsymbol{r_e}, \boldsymbol{r}_h) = \frac{1}{\sqrt{V}} e^{i\boldsymbol{K}\cdot\boldsymbol{R}} \phi_{1s}(r_e - \boldsymbol{r}_h) \quad \text{(S12)}$$

where $\phi_{1s}(\boldsymbol{r})$ is the hydrogen ground state wavefunction with exciton Bohr radius $a_x$. (Eq. S13)

$$\phi_{1s}(r) = \frac{2}{{a_x}^{3/2}} e^{-r/a_x} \frac{1}{\sqrt{4\pi}} \quad \text{(S13)}$$

Here, $a_x = a_o\, \varepsilon/\mu$, where $a_o$ is the hydrogen Bohr radius, $\mu$ is the reduced exciton mass, with corresponding binding energy ($B_x$) calculated by Eq. S14, where $Ry$ is the Rydberg.

$$B_x = \frac{\mu}{\epsilon^2} Ry = \frac{\hbar^2}{2\mu a_x^2} = \frac{1}{2}\frac{e^2}{\epsilon a_x} \quad \text{(S14)}$$

**Excitons in confined systems**

For an exciton confined to a nanocrystal, the effective mass equations are solved subject to the requirement that the wavefunction vanishes at the nanocrystal surface.

**Strong confinement**

When the exciton Bohr radius ($a_x$) is much larger than the nanocrystal size ($L$), the strong confinement regime is employed in which correlated motion of the electron and hole can be neglected. In this case, for a cube-shaped nanocrystal of edge length, $L$, the envelope function of the exciton can be written as the product of electron and hole wavefunctions as Eq. S15,

$$f(\boldsymbol{r_e}, \boldsymbol{r_h}) = \psi_{gr}(\boldsymbol{r_e})\psi_{gr}(\boldsymbol{r_h}) \quad \text{(S15)}$$

where ground-state wavefunctions of electrons, $\psi_{gr}(r_e)$, and holes, $\psi_{gr}(r_h)$, are given by Eq. S16,

$$\psi_{gr}(x, y, z) = (2/L)^{3/2}\cos(\pi x/L)\cos(\pi y/L)\cos(\pi z/L) \quad \text{(S16)}$$

The exciton energy relative to the bandgap ($E_g$) is found by computing the expectation value of the two-particle Hamiltonian (Eq. S11). The result is found as Eq. S17,[26]

$$E_x^{Strong} = E_g + \frac{\hbar^2}{2\mu}\left(\frac{3\pi^2}{L^2}\right) - 3.05\frac{e^2}{\epsilon_{in}L}$$

$$= E_g + B_x\left[\frac{3\pi^2}{\left(L/a_x\right)^2} - 2 \times 3.05 \times \frac{a_x}{L}\right] \quad \text{(S17)}$$

Here $\mu$ is the reduced mass of the exciton, $1/\mu = 1/m_e + 1/m_h$ and $\epsilon_{in}$ is the dielectric constant in the nanocrystal. The next term, which scales with size as $1/L^2$, is the kinetic energy of the electron and hole while the third term is the energy of their Coulomb attraction, calculated in first order perturbation theory. In the second line of the equation, the energy has been recast in terms of the ratio of the nanocrystal size to the exciton radius and parameterized in terms of $B_x$ that is defined in Eq. S14.

**Weak confinement**

In the case that $L$ is much larger than $a_x$, the weak confinement regime, where the electron and hole motion are strongly correlated, is realized. In this case, the plane wave envelope associated with bulk exciton states (Eq. S12) is replaced by a confined particle-in-a-box function. For the ground-state exciton in the weak confinement regime, the exciton envelope wavefunction is therefore given by (Eq. S18).

$$f(\boldsymbol{r}_e, \boldsymbol{r}_h) = \phi_{1s}(\boldsymbol{r_e} - \boldsymbol{r}_h)\,\psi_{gr}(\boldsymbol{R}) \quad \text{(S18)}$$

The relative wavefunction is simply the ground state hydrogenic function while the ground center of mass wavefunction is that of a particle-in-a-box. The energy relative to the bandgap of the ground state in a cube-shaped NC in the weak confinement regime is then described as Eq. S19,[26] where the total exciton effective mass is $M_x = m_e + m_h$:

$$E_x^{Weak} = E_g + \frac{\hbar^2}{2M_x}\left(\frac{3\pi^2}{L^2}\right) - B_x$$

$$= E_g + B_x\left\{\frac{\mu}{M_x}\left[\frac{3\pi^2}{\left(L/a_x\right)^2}\right] - 1\right\} \quad \text{(S19)}$$

**Intermediate confinement**

Nanocrystals with $L \sim a_x$ are in the intermediate confinement regime, where confinement effects on the carrier energies are significant but the motion of the electron and hole are correlated to such a degree that the strong confinement treatment of the Coulomb binding of the

electron and hole is inadequate. To model this, we write the envelope function of the confined excitons using a one-parameter ansatz function, Eq. S20.[26,27]

$$f(r_e, r_h) = \frac{1}{\sqrt{N(\beta)}} e^{-\beta|r_e - r_h|} \psi_{gr}(\boldsymbol{r}_e)\psi_{gr}(\boldsymbol{r}_h) \quad \text{(S20)}$$

The term $\psi_{gr}$ is the confined wavefunction for carriers in the strong confinement limit (Eq. S16) and therefore satisfies the boundary condition that the envelope function vanishes at the nanocrystal surface, while the term involving $\beta$, the variational parameter, has the form of the hydrogenic relative motion of the electron and hole, and builds correlation of the electron-hole motion into the wavefunction. In the expression, $N(\beta)$ is a normalization factor, determined by the condition Eq. S21,

$$\iint d^3 r_e d^3 r_h f^2(r_e, r_h) = 1 \quad \text{(S21)}$$

where the integration is performed over the volume of the nanocrystal. In the variational approach we calculate the expectation value of the two-particle Hamiltonian (Eq. S11) in a cube with $L$ and minimize this with respect to $\beta$. This procedure is done numerically and is described in the literature.[26,27]

**Exciton energy versus size for parabolic bands**

Using the results developed above, we show the exciton energy for the strong, weak, and intermediate confinement limits in an idealized simple parabolic band system in Figure S4. There, the exciton energy, $E_x$, relative to the bulk bandgap, $E_g$, is plotted in units of the exciton binding energy, $B_x$ versus $L/a_x$, the ratio of the edge length, $L$ of a cube-shaped NC to the exciton radius $a_x$. From the plots, it is clear that for $L < \sim 2a_x$ the energy calculated using the intermediate confinement wavefunction, Eq. S20, converges to the strong confinement result, while for $L > \sim 7a_x$ it converges to that calculated in the weak confinement limit. Inspection of the figure makes clear that for sizes $L > 3a_x$ the strong confinement model fails to accurately capture the Coulomb binding of the exciton, which drives the exciton energy below the bulk bandgap. Since perovskite NCs have exciton radii in the 3-4 nm size range,[28] this fact necessitates use of an intermediate confinement model for perovskite NCs for sizes $L > 9$ nm.

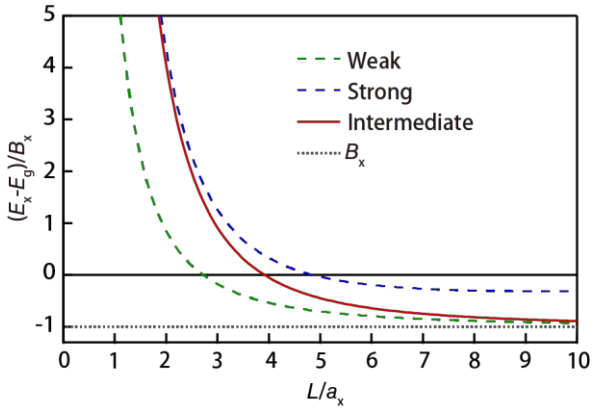


**Figure S4.** Exciton energy versus size for different confinement regimes in a parabolic band model. Exciton energy relative to the bulk bandgap ($E_x$-$E_g$) is plotted in units of the exciton binding energy ($B_x$) versus the ratio of the edge length of a cube-shaped nanocrystal to the exciton radius ($L/a_x$). The solid red line represents the result of a variational calculation valid for the intermediate confinement limit, $L \sim a_x$. Also shown for reference are the calculated exciton energies in the strong confinement regime ($L < a_x$, blue dashed line), the weak confinement regime ($L >> a_x$; green dashed line), and the exciton binding energy (black dotted line).

**Calculations for $CsPbBr_3$ Nanocrystals**

As a calibration of the quantum size level model developed for $CsPbI_3$ nanocrystals, described in the main text, we also calculated the size-dependent exciton energies of $CsPbBr_3$ nanocrystals and compared our model to data available in the literature. We begin the discussion of this effort by first reviewing the current status of the literature pertaining to modelling of exciton confinement energy versus nanocrystal size for the heavily studied $CsPbBr_3$ system.

Notwithstanding the discussion in the previous section, all studies that we are aware of thus far in the literatures which systematically investigate exciton confinement energy versus nanocrystal size for $CsPbBr_3$ NCs (or any other metal halide perovskite nanocrystal material) have employed the strong confinement approximation. The first such study, by Protesescu et al., compared a strong confinement model with measured room temperature PL energies versus sizes for approximately cube shaped NCs.[29] The model utilized the parabolic band approximation using effective mass parameters determined for bulk $CsPbBr_3$ by density functional theory (DFT) determined as $m_e = 0.14$, $m_h = 0.15$ for an exciton reduced mass of $\mu = 0.072$.[29] A more recent calculation by Rossi et al.[30], utilized the Kang Wise strong confinement model,[31] which captures band non-parabolicity effects. This published calculation, like the Protesescu model, also utilized effective mass parameters determined using DFT.[30] Using the parameters from Rossi et al., and

the expressions for the band edge effective masses in the literature[27], we find the band edge effective masses corresponding to the Rossi model parameters to be $m_e$= 0.121, $m_h$ = 0.117 for an exciton reduced mass of $\mu$ =0.060. Both of these models significantly overestimate the exciton energy because the band edge effective masses, determined in both cases using DFT, are a factor of ~ 2 smaller than the measured value of $\mu$ =0.126 for bulk $CsPbBr_3$.[28] Additionally, none of these models take account of the Coulomb interaction between the electron and the hole. In the next sub-section, we will describe the calculation of the exciton energy in $CsPbBr_3$ NCs which correctly accounts for this Coulomb interaction, using measured bulk effective mass parameters rather than parameters determined using DFT.

**Model based on measured effective mass parameters and accounting for e/h interaction**

Given the deficiencies of the published models for exciton energies in $CsPbBr_3$ nanocrystals discussed in the last section, we calculated the size-dependent exciton energies of $CsPbBr_3$ nanocrystals using measured bulk effective mass parameters rather than parameters based on density functional theory calculations and accounting for the electron-hole Coulomb interaction. We compare our calculations against the published exciton absorption data from Brennan et al.[32] For these calculations, we used dielectric constant ($\epsilon_{eff}$) and Kane energy ($E_p$) determined from low temperature exciton magneto-transmission measurements on bulk orthorhombic $CsPbBr_3$ reported by Yang et al.[28] The bulk bandgap parameter, $E_g$, was adjusted to achieve best fit to the measured room temperature $CsPbBr_3$ nanocrystal absorption peak energy versus nanocrystal size data of Brennan et al.,[32] shown in Figure S5 alongside the fit. The parameters used in the calculation are summarized in Table S6.

In Figure S5, we show calculated size dependence in the strong confinement approximation assuming parabolic band dispersion (blue line), the intermediate confinement approximation calculated for parabolic band dispersion (red line), and the intermediate confinement approximation calculated for a coupled-band model, taking account of conduction-to-valence band coupling in the context of the Kang and Wise model (purple).[31,33] This model, which accounts for the *s*- to *p*- coupling between conduction and valence band quantum size levels, was implemented by using energy dependent effective masses according to Eq. 6 of the main text, derived in the report by Sercel et al.,[33] which closely matches the full Kang-Wise model for spherical nanocrystals of radius $a_{eff} = L / \sqrt{3}$. The correspondence $a_{eff} = L / \sqrt{3}$ is based

on matching the energy of a cube shaped nanocrystal to that of a spherical nanocrystal in strong confinement. The figure also shows that the parabolic dispersion models significantly overestimate the exciton absorption energy for small-sized nanocrystals while the strong confinement approximation does not correctly capture the exciton binding energy at large size, as expected. The best fit requires a bulk bandgap, $E_g$, approximately 50 meV larger than the 270 K bandgap reported by Yang and coworkers.[28]

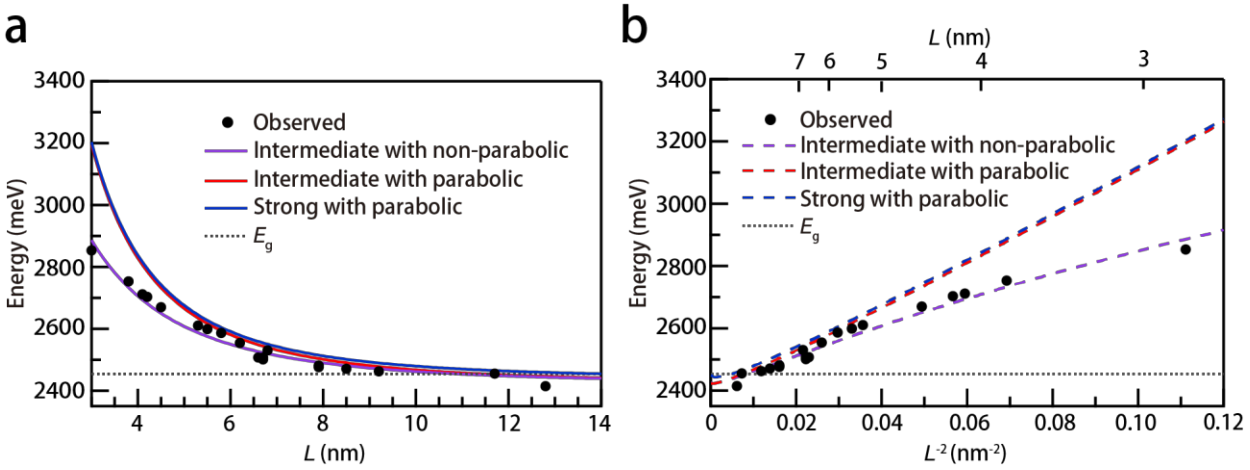


**Figure S5.** (a and b) Measured vs calculated sizing curves for $CsPbBr_3$ nanocrystals. Model calculations in the strong confinement regime in the parabolic approximation, and the intermediate confinement regime within the parabolic and non-parabolic approximations, are presented with the blue, red and purple lines, respectively. The measured data shown as solid circles are from Brennan et al.[32] The calculated lines were drawn in two ways: $CsPbBr_3$ NC absorption peak energy versus NC size $L$ (solid lines in a) and the absorption peak energy plotted versus the inverse square of NC size $1/L^2$ (dashed lines in b) to better illustrate the departure from linearity of energy plotted versus $1/L^2$ expected in the parabolic approximation. The model parameters are derived from 2K magneto-transmission measurements on bulk $CsPbBr_3$,[28] with the exception of the bandgap which is adjusted to achieve the best fit to the measured data.

**Table S6** Summary of electronic structure parameters used for $CsPbBr_3$ nanocrystals. The Kane energy was extracted from a 2-band fit to the reduced effective mass and dielectric constant of bulk $CsPbBr_3$ at T=2K reported by Yang and co-workers.[28] The bandgap was determined by the best fit to the room temperature nanocrystal absorption data reported by Brennan and co-workers.[32] All other parameters are measured values from the literature.[28]

| Parameter | Value |
|---|---|
| Bandgap $E_g$ | 2.454 eV |
| Kane energy $E_p$ | 27.88 eV |
| Exciton reduced mass $\mu$ | 0.132 |
| Dielectric constant $\epsilon_{eff}$ | 7.3 |
| Exciton radius $a_x$ | 2.93 nm |
| Exciton binding energy $B_x$ | 33.6 meV |

**Lattice strain effect calculations**

The lattice constants measured versus nanocrystal size, given in Table S4 and shown in Figure 3 of the main text, are different from the bulk lattice constants (given in the caption of Figure S2). As a result, the unit cell volume ($V_c$) varies as a function of $L$. The resulting unit cell volume dilatation relative to the bulk ($\Delta V_c/V_{c,bulk}$) can be viewed as a strain and is expected to impact the bandgap parameter, $E_g$, via the deformation potential shown in Eq. S22.

$$\Delta E_g = \alpha_V \frac{\Delta V_c}{V_{c,bulk}} \quad \text{(S22)}$$

The volume deformation potential is given by Eq. S23,[34] from which we can compute the bandgap shift associated with a given unit cell volume dilatation ($\Delta V_c/V_{c,bulk}$).

$$\alpha_v \equiv \frac{dE_g}{dLnV} = V\frac{dE_g}{dV} \quad \text{(S23)}$$

To carry out this calculation we use the pressure deformation potential for $CsPbI_3$ nanocrystals measured in the literature[35] of $\alpha_p = 1.4\times10^{-2}$ eV/GPa. We note that the pressure deformation potential and the volume deformation potential are related through the bulk modulus, $B = -V\mathrm{d}P/\mathrm{d}V$, as shown in Eq. S24.

$$\alpha_P \equiv \frac{dE_g}{dP} = -\frac{\alpha_v}{K} \quad \text{(S24)}$$

Using the bulk modulus B= 16 GPa calculated in density functional theory for $CsPbI_3$ in the cubic perovskite phase,[22] we find the volume deformation potential $\alpha_V$ = 0.22 eV, substantially smaller than the 2 eV value calculated by Frost et al.[34] As a check, the bulk

modulus for $CsPbI_3$ measured in the non-perovskite $\delta$ phase by Rakita et al.[23] is K = 19.8 GPa, leading to $\alpha_V$ = 0.28 eV. In Figure S3 we show the unit cell volume dilatation versus $1/L$, calculated using the lattice parameters in Table S4 and the bulk lattice parameters given in Figure S2. Using the calculated unit cell volume dilatation, we determined the bandgap shift vs $1/L$ using $\alpha_V$ = 0.22 eV , shown in Figure S6. A linear interpolation is given in Eq. S25.

$$\Delta E_g(L) = 26.4\ meV \times \frac{1\ (nm)}{L\ (nm)} \quad \text{(S25)}$$

For the small sized NCs (5.7nm) the bandgap shift is ~ 4.6 meV. This degree of dilatation-induced bandgap shift is almost negligible; nevertheless, we evaluated the effect of the volume dilatation on the model sizing curves and the best-fit parameter values shown in Figure S7 and Table S7, respectively. Inspection of the best-fit parameter values in Table S7 shows that inclusion of the strain effect results in a slight increase of the exciton reduced mass $\mu$ (from 0.159 to 0.163), reflecting the fact that the exciton energy increase with decreasing size is partly due to the strain effect calculated here.

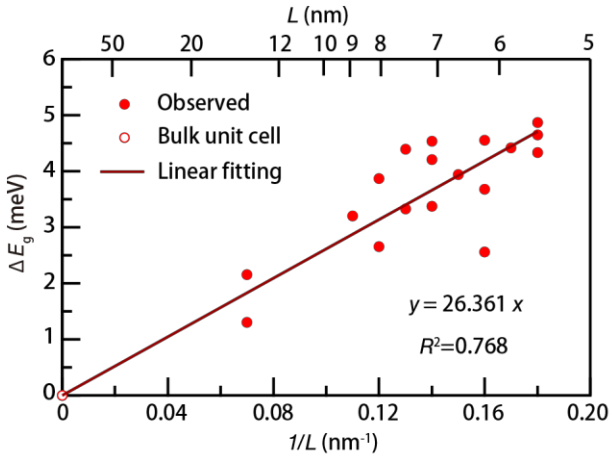


**Figure S6.** The bandgap shift relative to the bulk, unstrained bandgap is plotted versus $1/L$. The values calculated with a volume deformation potential model for each sample (solid circle) are fitted to a linear function (sold line), whose equation is given in Eq. S25. The value for the bulk unit cell (hollow circle) unstrained crystal is calculated using the linear fit in Figure S3 with the deformation potential $\alpha_V$ = 0.22 eV.

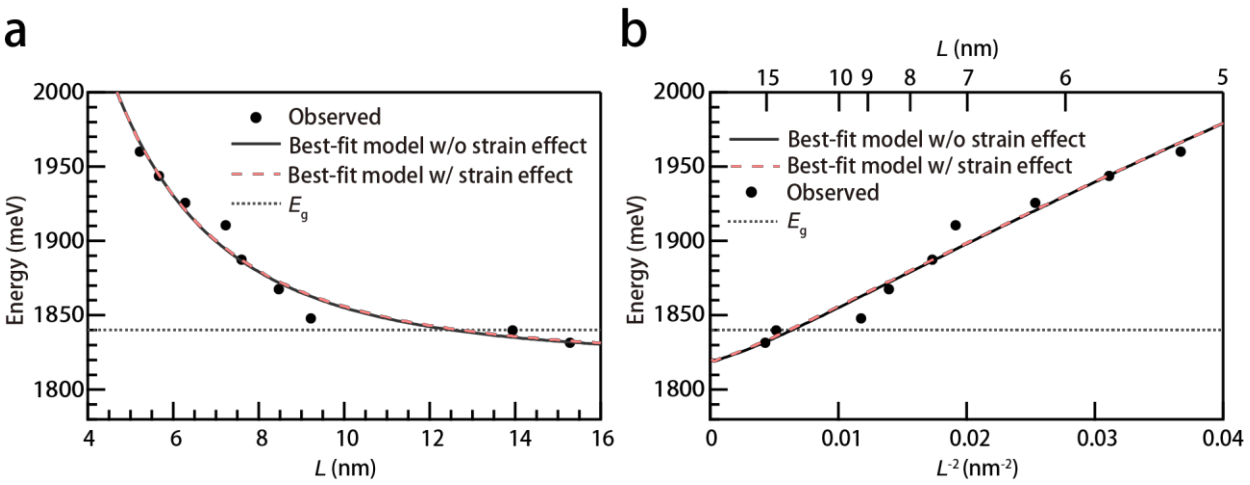


**Figure S7.** Measured vs calculated sizing curves fitted using the best model with (pink dotted line) and without (black solid line) strain effect. The measured absorption peak energies are plotted versus $L$ (a) and $1/L^2$ (b), respectively. Measured 300K data are shown as solid circle points in the figures. The theoretical curves shown are calculated using the intermediate confinement model with band non-parabolicity effects. Parameters used in these plots are summarized in Table S7.

**Table S7** Summary of electronic structure parameters for the best-fit model of $CsPbI_3$ NC absorption energy, with and without strain effect. The best-fit values are determined by fitting to the $CsPbI_3$ absorption data as shown in Figure S7. The dielectric constant is constrained to the value measured for bulk $\alpha$ phase $CsPbI_3$ in the reported by Yang and coworkers.[28]

| Parameter | Best-fit without strain | Best-fit with strain |
|---|---|---|
| Bandgap $E_g$ | 1.840 eV | 1.840 eV |
| Kane energy $E_p$ | 17.4 eV | 17.0 eV |
| Exciton reduced mass $\mu$ | 0.159 | 0.163 |
| Dielectric constant $\epsilon_{eff}$ | 10 (constrained) | 10 (constrained) |
| Exciton radius $a_x$ | 3.33 nm | 3.25 nm |
| Exciton binding energy $B_x$ | 21.2 meV | 22.1 meV |

**References:**


(1) Hazarika, A.; Zhao, Q.; Gaulding, E. A.; Christians, J. A.; Dou, B.; Marshall, A. R.; Moot, T.; Berry, J. J.; Johnson, J. C.; Luther, J. M. Perovskite Quantum Dot Photovoltaic Materials beyond the Reach of Thin Films: Full-Range Tuning of A-Site Cation Composition. *ACS Nano* **2018**, 12, 10327–10337.

(2) Wheeler, L. M.; Sanehira, E. M.; Marshall, A. R.; Schulz, P.; Suri, M.; Anderson, N. C.; Christians, J. A.; Nordlund, D.; Sokaras, D.; Kroll, T.; et al. Targeted Ligand-Exchange Chemistry on Cesium Lead Halide Perovskite Quantum Dots for High-Efficiency Photovoltaics. *J. Am. Chem. Soc*. **2018**, 140, 10504–10513

(3) Brennan, M. C.; Kuno, M.; Rouvimov, S. Crystal Structure of Individual CsPbBr3 Perovskite Nanocubes. *Inorg. Chem*. **2019**, 58, 1555–1560.

(4) Shang, Q.; Kaledin, A. L.; Li, Q.; Lian, T. Size Dependent Charge Separation and Recombination in $CsPbI_3$ Perovskite Quantum Dots. *J. Chem. Phys.* **2019**, *151*, 74705.

(5) Veldhuis, S. A.; Ng, Y. F.; Ahmad, R.; Bruno, A.; Jamaludin, N. F.; Damodaran, B.; Mathews, N.; Mhaisalkar, S. G. Crown Ethers Enable Room-Temperature Synthesis of $CsPbBr_3$ Quantum Dots for Light-Emitting Diodes. *ACS Energy Lett.* **2018**, *3*, 526–531.

(6) Chang, Y.; Yoon, Y. J.; Li, G.; Xu, E.; Yu, S.; Lu, C.-H.; Wang, Z.; He, Y.; Lin, C. H.; Wagner, B. K.; et al. All-Inorganic Perovskite Nanocrystals with a Stellar Set of Stabilities and Their Use in White Light-Emitting Diodes. *ACS Appl. Mater. Interfaces* **2018**, *10*, 37267–37276.

(7) Yuan, X.; Hou, X.; Li, J.; Qu, C.; Zhang, W.; Zhao, J.; Li, H. Thermal Degradation of Luminescence in Inorganic Perovskite $CsPbBr_3$ Nanocrystals. *Phys. Chem. Chem. Phys.* **2017**, *19*, 8934–8940.

(8) Ghosh, D.; Ali, M. Y.; Chaudhary, D. K.; Bhattacharyya, S. Dependence of Halide Composition on the Stability of Highly Efficient All-Inorganic Cesium Lead Halide Perovskite Quantum Dot Solar Cells. *Sol. Energy Mater. Sol. Cells* **2018**, *185*, 28–35.

(9) Du, X.; Wu, G.; Cheng, J.; Dang, H.; Ma, K.; Zhang, Y.-W.; Tan, P.-F.; Chen, S. High-Quality $CsPbBr_3$ Perovskite Nanocrystals for Quantum Dot Light-Emitting Diodes. *RSC Adv.* **2017**, *7*, 10391–10396.

(10) Park, Y. S.; Guo, S.; Makarov, N. S.; Klimov, V. I. Room Temperature Single-Photon Emission from Individual Perovskite Quantum Dots. *ACS Nano* **2015**, *9*, 10386–10393.

(11) Li, Z.; Kong, L.; Huang, S.; Li, L. Highly Luminescent and Ultrastable $CsPbBr_3$ Perovskite Quantum Dots Incorporated into a Silica/Alumina Monolith. *Angew. Chemie Int. Ed.* **2017**, *56*, 8134–8138.

(12) Bi, C.; Kershaw, S. V; Rogach, A. L.; Tian, J. Improved Stability and Photodetector Performance of $CsPbI_3$ Perovskite Quantum Dots by Ligand Exchange with Aminoethanethiol. *Adv. Funct. Mater.* **2019**, *29*, 1902446.

(13) Ravi, V. K.; Swarnkar, A.; Chakraborty, R.; Nag, A. Excellent Green but Less Impressive Blue Luminescence from $CsPbBr_3$ perovskite Nanocubes and Nanoplatelets. *Nanotechnology* **2016**, *27*, 325708.

(14) Liu, C.; Hu, M.; Zhou, X.; Wu, J.; Zhang, L.; Kong, W.; Li, X.; Zhao, X.; Dai, S.; Xu, B.; et al. Efficiency and Stability Enhancement of Perovskite Solar Cells by Introducing $CsPbI_3$ Quantum Dots as an Interface Engineering Layer. *NPG Asia Mater.* **2018**, *10*, 552–561.

(15) Huang, Y.; Fang, M.; Zou, G.; Zhang, B.; Wang, H. Monochromatic and Electrochemically Switchable Electrochemiluminescence of Perovskite $CsPbBr_3$ Nanocrystals. *Nanoscale* **2016**, *8*,

18734–18739.

(16) Zhou, W.; Sui, F.; Zhong, G.; Cheng, G.; Pan, M.; Yang, C.; Ruan, S. Lattice Dynamics and Thermal Stability of Cubic-Phase $CsPbI_3$ Quantum Dots. *J. Phys. Chem. Lett.* **2018**, *9*, 4915–4920.

(17) Li, C.; Zang, Z.; Chen, W.; Hu, Z.; Tang, X.; Hu, W.; Sun, K.; Liu, X.; Chen, W. Highly Pure Green Light Emission of Perovskite $CsPbBr_3$ Quantum Dots and Their Application for Green Light-Emitting Diodes. *Opt. Express* **2016**, *24*, 15071–15078.

(18) Sutton, R. J.; Filip, M. R.; Haghighirad, A. A.; Sakai, N.; Wenger, B.; Giustino, F.; Snaith, H. J. Cubic or Orthorhombic? Revealing the Crystal Structure of Metastable Black-Phase $CsPbI_3$ by Theory and Experiment. *ACS Energy Lett.* **2018**, *3*, 1787–1794.

(19) Weissmüller, J.; Cahn, J. W. Mean Stresses in Microstructures Due to Interface Stresses: A Generalization of a Capillary Equation for Solids. *Acta Mater.* **1997**, *45*, 1899–1906.

(20) Diehm, P. M.; Ágoston, P.; Albe, K. Size-Dependent Lattice Expansion in Nanoparticles: Reality or Anomaly? *ChemPhysChem* **2012**, *13*, 2443–2454.

(21) Huang, Z.; Thomson, P.; Di, S. Lattice Contractions of a Nanoparticle Due to the Surface Tension: A Model of Elasticity. *J. Phys. Chem. Solids* **2007**, *68*, 530–535.

(22) Jong, U.-G.; Yu, C.-J.; Kye, Y.-H.; Kim, Y.-S.; Kim, C.-H.; Ri, S.-G. A First-Principles Study on the Chemical Stability of Inorganic Perovskite Solid Solutions $Cs_{1-x}Rb_xPbI_3$ at Finite Temperature and Pressure. *J. Mater. Chem. A* **2018**, *6*, 17994–18002.

(23) Rakita, Y.; Cohen, S. R.; Kedem, N. K.; Hodes, G.; Cahen, D. Mechanical Properties of $APbX_3$ (A = Cs or $CH_3NH_3$; X = I or Br) Perovskite Single Crystals. *MRS Commun.* **2015**, *5*, 623–629.

(24) E. Pikus, G.; L. Bir, G. Exchange Interaction in Excitons in Semiconductors. *Sov. Phys. JETP* **1971**, *33,* 108-114.

(25) Bir, G. L.; Pikus, G. E. *Symmetry and Strain-Induced Effects in Semiconductors*; A Halsted Press book; Wiley, New York, New York **1974**.

(26) Sercel, P. C.; Lyons, J. L.; Wickramaratne, D.; Vaxenburg, R.; Bernstein, N.; Efros, A. L. Exciton Fine Structure in Perovskite Nanocrystals. *Nano Lett.* **2019**, *19*, 4068–4077.

(27) Becker, M. A.; Vaxenburg, R.; Nedelcu, G.; Sercel, P. C.; Shabaev, A.; Mehl, M. J.; Michopoulos, J. G.; Lambrakos, S. G.; Bernstein, N.; Lyons, J. L.; et al. Bright Triplet Excitons in Caesium Lead Halide Perovskites. *Nature* **2018**, *553*, 189.

(28) Yang, Z.; Surrente, A.; Galkowski, K.; Miyata, A.; Portugall, O.; Sutton, R. J.; Haghighirad, A. A.; Snaith, H. J.; Maude, D. K.; Plochocka, P.; et al. Impact of the Halide Cage on the Electronic Properties of Fully Inorganic Cesium Lead Halide Perovskites. *ACS Energy Lett.* **2017**, *2*, 1621–1627.

(29) Protesescu, L.; Yakunin, S.; Bodnarchuk, M. I.; Krieg, F.; Caputo, R.; Hendon, C. H.; Yang, R. X.; Walsh, A.; Kovalenko, M. V. Nanocrystals of Cesium Lead Halide Perovskites ($CsPbX_3$, X = Cl, Br, and I): Novel Optoelectronic Materials Showing Bright Emission with Wide Color Gamut. *Nano Lett.* **2015**, *15*, 3692–3696.

(30) Rossi, D.; Wang, H.; Dong, Y.; Qiao, T.; Qian, X.; Son, D. H. Light-Induced Activation of Forbidden Exciton Transition in Strongly Confined Perovskite Quantum Dots. *ACS Nano* **2018**, *12*, 12436− 12443.

(31) Kang, I.; Wise, F. W. Electronic Structure and Optical Properties of PbS and PbSe Quantum Dots. *J. Opt. Soc. Am. B* **1997**, *14*, 1632–1646.

(32) Brennan, M. C.; Herr, J. E.; Nguyen-Beck, T. S.; Zinna, J.; Draguta, S.; Rouvimov, S.; Parkhill, J.;

Kuno, M. Origin of the Size-Dependent Stokes Shift in $CsPbBr_3$ Perovskite Nanocrystals. *J. Am. Chem. Soc.* **2017**, *139*, 12201–12208.

(33) Sercel, P. C.; Lyons, J. L.; Bernstein, N.; Efros, A. L. Quasicubic Model for Metal Halide Perovskite Nanocrystals, *J. Chem. Phys.* **2019**, *151*, 234106.

(34) Frost, J. M.; Butler, K. T.; Brivio, F.; Hendon, C. H.; van Schilfgaarde, M.; Walsh, A. Atomistic Origins of High-Performance in Hybrid Halide Perovskite Solar Cells. *Nano Lett.* **2014**, *14*, 2584–2590.

(35) Beimborn, J. C.; Hall, L. M. G.; Tongying, P.; Dukovic, G.; Weber, J. M. Pressure Response of Photoluminescence in Cesium Lead Iodide Perovskite Nanocrystals. *J. Phys. Chem. C* **2018**, *122*, 11024–11030.